Article

Distribution control enables efficient reduced-dimensional perovskite LEDs

https://doi.org/10.1038/s41586-021-03997-z

Received: 22 April 2020

Accepted: 5 September 2021

Published online: 24 November 2021

Check for updates

Dongxin Ma[1], Kebin Lin[2], Yitong Dong[1], Hitarth Choubisa[1], Andrew H. Proppe[1], Dan Wu[3], Ya-Kun Wang[1], Bin Chen[1], Peicheng Li[4], James Z. Fan[1], Fanglong Yuan[1,4], Andrew Johnston[1], Yuan Liu[1], Yuetong Kang[5,6], Zheng-Hong Lu[4], Zhanhua Wei[2]✉ & Edward H. Sargent[1]✉

Light-emitting diodes (LEDs) based on perovskite quantum dots have shown external quantum efficiencies (EQEs) of over 23% and narrowband emission, but suffer from limited operating stability[1]. Reduced-dimensional perovskites (RDPs) consisting of quantum wells (QWs) separated by organic intercalating cations show high exciton binding energies and have the potential to increase the stability and the photoluminescence quantum yield[2,3]. However, until now, RDP-based LEDs have exhibited lower EQEs and inferior colour purities[4–6]. We posit that the presence of variably confined QWs may contribute to non-radiative recombination losses and broadened emission. Here we report bright RDPs with a more monodispersed QW thickness distribution, achieved through the use of a bifunctional molecular additive that simultaneously controls the RDP polydispersity while passivating the perovskite QW surfaces. We synthesize a fluorinated triphenylphosphine oxide additive that hydrogen bonds with the organic cations, controlling their diffusion during RDP film deposition and suppressing the formation of low-thickness QWs. The phosphine oxide moiety passivates the perovskite grain boundaries via coordination bonding with unsaturated sites, which suppresses defect formation. This results in compact, smooth and uniform RDP thin films with narrowband emission and high photoluminescence quantum yield. This enables LEDs with an EQE of 25.6% with an average of 22.1 ±1.2% over 40 devices, and an operating half-life of two hours at an initial luminance of 7,200 candela per metre squared, indicating tenfold-enhanced operating stability relative to the best-known perovskite LEDs with an EQE exceeding 20%[1,4–6].

Metal-halide perovskites hold promise in solar cell[7], laser[8], photodetector[9] and light-emission applications[10]. They feature a combination of structural diversity, a tunable bandgap, saturated emission colours, superior luminescence efficiencies, low-cost solution processing and high charge mobilities. The rapid development of perovskite light-emitting diodes (LEDs) has enabled an external quantum efficiency (EQE) of 23.4% at green wavelengths with a full-width at half-maximum of 20 nm (ref. [1]). However, this has not yet matched the performance of inorganic quantum dot[11,12] and organic[13,14] LEDs, and the operating half-life at an initial luminance of 1,000 cd m^{-2} has so far been limited to 7 min (ref. [1]).

Organic–inorganic hybrid reduced-dimensional perovskites (RDPs) have emerged as a means to increase stability. RDPs consist of perovskite flakes separated by bilayers of organic intercalating cations such as butylammonium (BTA) and phenylethylammonium (PEA). These bind to halide-rich surfaces, protecting perovskite surfaces and improving stability[5,6]. RDPs show higher exciton binding energies than their bulk counterparts, and exciton confinement that enables increased radiative recombination rates and enhanced photoluminescence quantum yields (PLQYs)[15–17]. RDPs form with a mixture of quantum well (QW) thicknesses and therefore bandgaps[18], leading to funnelling of injected carriers via rapid interwell carrier transfer[19,20]; however, so far, RDP-based green LEDs have been limited to lower efficiencies and colour purities[4–6]. We ascribed this to the inferior control over the QW thickness uniformity across the ensemble, leading to the presence of strongly confined QWs in an otherwise homogenous distribution, thereby causing spatial and energetic disorder.

The QW polydispersity depends on the diffusion of the organic intercalating cations during RDP film deposition. RDPs synthesized using smaller cations such as BTA show greater QW-thickness polydispersity than those made using bulkier cations such as PEA—a finding ascribed to the faster diffusion of BTA that leads to a higher probability of forming low-thickness QWs[19]. We sought further control over the diffusion of the organic cations and took the approach of using an additive as an experimental handle that could be controlled independently of the organic cations.

[1]Department of Electrical and Computer Engineering, University of Toronto, Toronto, Ontario, Canada. [2]Xiamen Key Laboratory of Optoelectronic Materials and Advanced Manufacturing, Institute of Luminescent Materials and Information Displays, College of Materials Science and Engineering, Huaqiao University, Xiamen, People's Republic of China. [3]College of New Materials and New Energies, Shenzhen Technology University, Shenzhen, People's Republic of China. [4]Department of Materials Science and Engineering, University of Toronto, Toronto, Ontario, Canada. [5]Department of Chemistry, University of Victoria, Victoria, British Columbia, Canada. [6]Present address: State Key Laboratory for Advanced Metals and Materials, School of Materials Science and Engineering, University of Science and Technology Beijing, Beijing, People's Republic of China. ✉e-mail: weizhanhua@hqu.edu.cn; ted.sargent@utoronto.ca

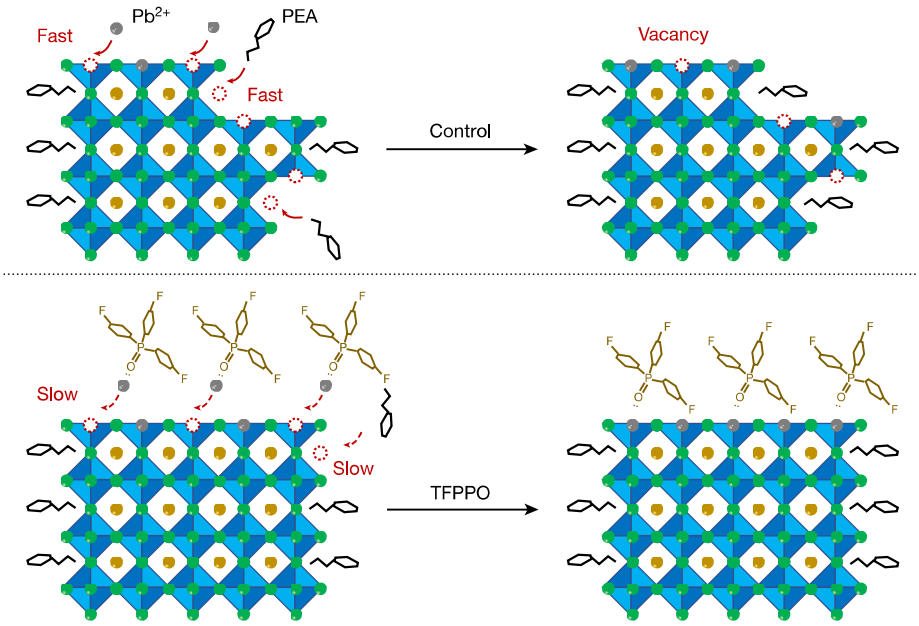

Fig. 1 | Distribution control strategy. During antisolvent-induced crystallization, $[PbBr_6]^{4-}$ nuclei, MA and Cs^+ cations assemble to form the perovskite flakes, allowing the PEA organic cations to diffuse and enter the extended perovskite lattice, thereby forming RDPs. In the control case, rapid diffusion of PEA leads to QW polydispersity, whereas in the case of crystallization with TFPPO added to the antisolvent, the fluorine atoms bind to PEA via hydrogen bonds, limiting their diffusion and promoting the formation of RDPs with monodispersed QWs. The P=O moiety additionally passivates the perovskite grain boundaries.

We sought to bind the organic cations—PEA in this case—with a molecular additive that would limit their diffusion during RDP film deposition, thereby suppressing the formation of low-*n* QWs (*n* describes the number of the corner-sharing $[PbBr_6]^{4-}$ octahedra perovskite flakes in a single well). We synthesized tris(4-fluorophenyl)phosphine oxide (TFPPO)—a molecular additive that we introduced via the antisolvent—which contains two functional groups: strongly electronegative fluorine atoms to form hydrogen bonds with the organic cations, serving as a diffusion controller during RDP film deposition, towards the goal of RDPs with energetically monodispersed QWs; and phosphine oxide (P=O) to bind the unsaturated sites at the perovskite grain boundaries, thus serving as a surface passivant to lower defect densities and enhance the PLQY (Fig. 1).

We focused on RDPs with a stoichiometry of $PEA_2Cs_{1.6}MA_{0.4}Pb_3Br_{10}$ and prepared thin films on glass substrates using a two-step spin-coating process (Methods; here MA is methylammonium). We used chloroform as the antisolvent in all studies, and a non-fluorinated additive, triphenylphosphine oxide (TPPO) for comparison. Grazing incidence wide-angle X-ray scattering (GIWAXS) measurements indicated that control RDPs prepared with the additive-free antisolvent showed well ordered structures, with QWs oriented predominantly parallel to the substrate, as previously observed for low-*n* QWs[19]; by contrast, both TPPO-treated and TFPPO-treated RDPs showed isotropic rings, the latter more homogeneous, suggesting more isotropic orientation of perovskite layers. Diffraction peaks present at $q_z \approx 0.5$ Å^{-1} and $q_z \approx 0.8$ Å^{-1} in the control RDPs were absent in TPPO-treated and TFPPO-treated RDPs, indicating suppression of low-*n* QWs (Extended Data Fig. 1a–c).

Control RDPs showed four distinctive bleach peaks in the transient absorption (TA) spectra, corresponding to the $n = 1$, $n = 3$, $n = 5$ and $n = 5+$ QWs, respectively[20] (Fig. 2a, d). TPPO-treated RDPs showed a prominent peak at 495 nm with a broad shoulder (Fig. 2b, e), whereas TFPPO-treated RDPs showed a narrower peak at 495 nm dominated by $n = 5+$ QWs (Fig. 2c, f). The narrowing and redshifting of the bleach peak at early delay times is consistent with carrier transfer from lower-to-higher-*n* RDPs in TFPPO-treated RDPs. The efficiency of carrier funnelling to the lowest bandgap RDP or bulk perovskite is evidenced by the narrower photoluminescence (PL) spectra (Fig. 2g–i), and enhanced radiative recombination efficiency is evidenced by the higher PLQY of TFPPO-treated RDPs (Extended Data Fig. 1d–f).

We then used time-correlated single-photon counting to investigate the charge-carrier kinetics of the RDPs, and found that TPPO-treated and TFPPO-treated RDPs showed longer radiative lifetimes than control RDPs (Extended Data Fig. 1g). We also measured the photostability, and observed that TFPPO-treated RDPs retained more than 50% of their original emission intensity after one hour of continuous excitation in a nitrogen-filled glovebox (Extended Data Fig. 1h)—tenfold longer than the half-life of control RDPs.

To understand the functions of the fluorine atoms and the P=O moiety, we prepared RDPs using two other additives: tris(4-fluorophenyl) phosphine (TFPP), the structure of which contains fluorine but no P=O; and triphenylphosphine (TPP), the structure of which has neither fluorine nor P=O. Compared with TPP-treated RDPs, TFPP-treated RDPs showed narrower TA and PL spectra, consistent with fluorine enhancing the QW monodispersity; TPPO-treated RDPs showed a higher PLQY than TPP-treated RDPs, consistent with the P=O moiety decreasing the defect densities via passivation of the perovskite grain boundaries[21,22] (Extended Data Fig. 2).

We used X-ray diffraction (XRD) to characterize the structure and ordering of the RDPs (Extended Data Fig. 1i). Control, TPPO-treated and TFPPO-treated RDPs showed successively wider XRD profiles with signals shifting towards smaller angles, as well as gradually decreasing crystalline sizes. Scanning electron microscope (SEM) and atomic force microscope (AFM) characterization indicated that TFPPO-treated RDPs showed improved film morphology compared with control and TPPO-treated RDPs (Extended Data Fig. 3).

We next studied the mechanism of diffusion control and surface passivation experimentally and computationally. We used nuclear magnetic resonance (NMR) to examine the interaction between TPPO, TFPPO and the perovskite precursor components in solutions. We dissolved TPPO and TFPPO in deuterated dimethyl sulfoxide, then added each perovskite

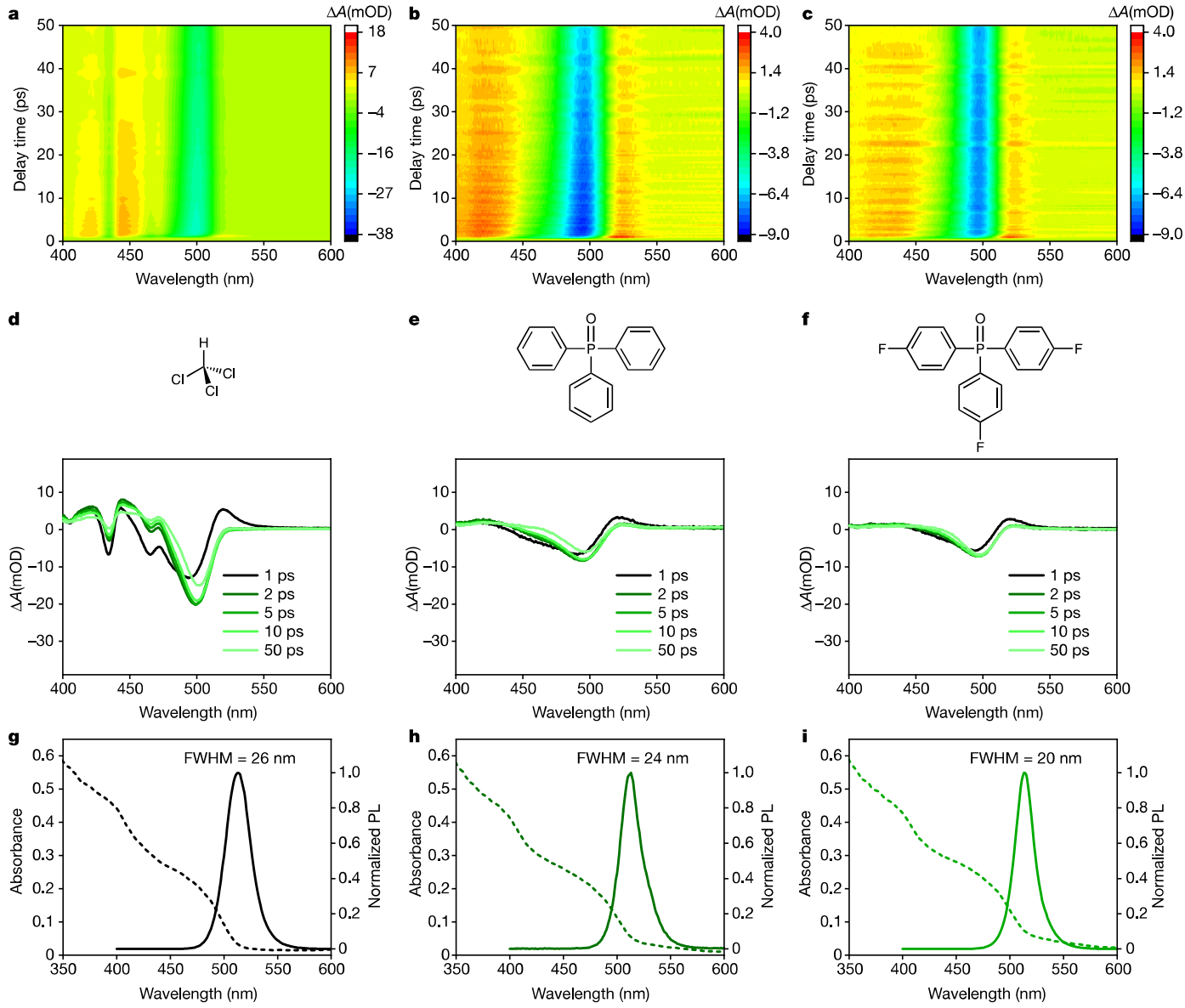

Fig. 2 | Optical characteristics. a–c, TA spectra of control (**a**), TPPO-treated (**b**) and TFPPO-treated (**c**) RDPs at a delay time ranging from 0 ps to 50 ps. **d–f**, TA spectra of control (**d**), TPPO-treated (**e**) and TFPPO-treated (**f**) RDPs at delay times of 1 ps, 2 ps, 5 ps, 10 ps and 50 ps, with the chemical structure of chloroform (antisolvent), TPPO and TFPPO, respectively, shown above. **g–i**, Absorption (dashed) and PL (solid) spectra of control (**g**), TPPO-treated (**h**) and TFPPO-treated (**i**) RDPs. FWHM, full-width at half-maximum.

precursor component (MABr, PEABr, CsBr or $PbBr_2$). Pure TPPO and TPPO with the addition of CsBr showed similar ^{31}P NMR signals, suggesting that there was little interaction between TPPO and CsBr; whereas the addition of $PbBr_2$, PEABr and MABr resulted in downfield-shifted signals. Similar results were observed in the case of TFPPO (Fig. 3a). This is consistent with the P=O moiety of TPPO and TFPPO forming coordination bonds with the Pb^{2+} cations (P=O:Pb), as well as hydrogen bonds with the ammonium tails of the organic cations (P=O···H–N), which withdraws electron density from the phosphorous atoms, thereby downfield-shifting the ^{31}P NMR signals. The addition of PEABr to pure TFPPO also led to downfield-shifted ^{19}F NMR signals, consistent with the fluorine atoms forming hydrogen bonds with PEA (F···H–N), increasing the steric hindrance and slowing its diffusion during RDP film deposition, thereby suppressing the formation of low-*n* QWs that consume more PEA[19].

We used X-ray photoelectron spectroscopy (XPS) and Fourier-transform infrared spectroscopy (FTIR) to investigate the interaction between TPPO, TFPPO and RDPs in thin films. Compared with control RDPs, TPPO-treated and TFPPO-treated RDPs showed core-level peaks of Pb 4*f* and Br 3*d* that were shifted towards lower binding energies (Fig. 3b, c). This demonstrates that the P=O moiety donates its lone electron pair on the oxygen atoms to the empty 6*p* orbital of Pb^{2+}, not only decreasing the cationic charge but also leading to a change in the electrostatic interaction between the Pb^{2+} and the Br^- ions[5]. In the FTIR spectra, we observed an infrared peak at 1,193 cm^{-1} arising from the P=O stretching vibration[23] for both pure TPPO and TFPPO, and found that this shifted to a lower wavenumber for TPPO-treated and TFPPO-treated RDPs (Fig. 3d, e). For pure TPPO and TPPO-treated RDPs, the peaks corresponding to *ν*(Ar–H)[24] at 1,437 cm^{-1} and *ν*(P–Ar)[23] at 1,119 cm^{-1} remained unchanged, indicating that there was little interaction between RDPs and the phenyl group of TPPO. However, the peaks corresponding to *ν*(Ar–F)[25] at 1,410 cm^{-1} and 1,247 cm^{-1} and *ν*(P–Ar) at 1,129 cm^{-1} for pure TFPPO all shifted to lower wavenumbers for TFPPO-treated RDPs, suggesting that the fluorine-derived hydrogen bonds (F···H–N) persisted in the fully formed thin films.

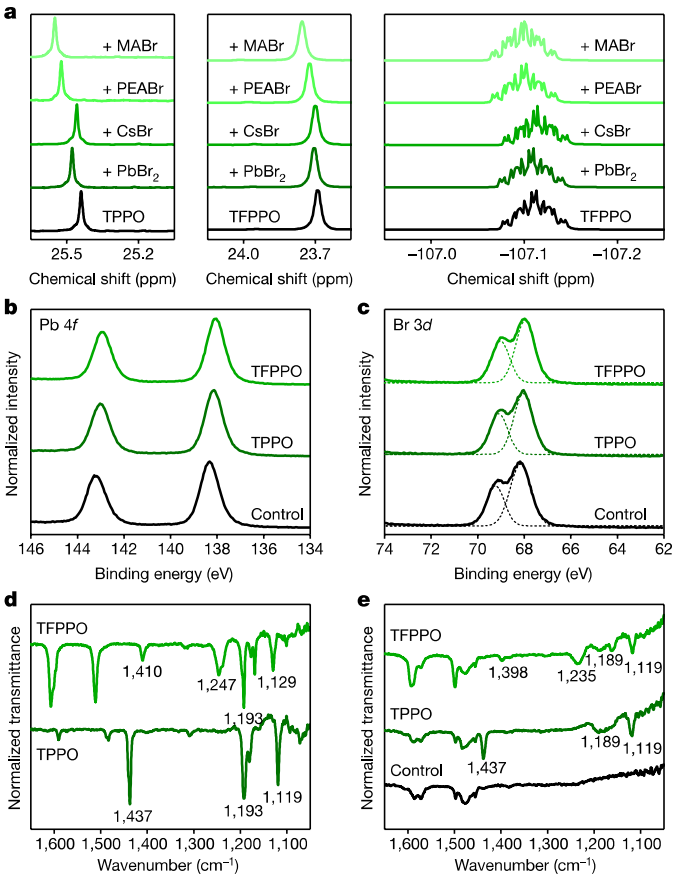

Fig. 3 | NMR, XPS and FTIR studies. a, Left: ^{31}P NMR spectra of pure TPPO and TPPO with different perovskite precursor components. Right: ^{31}P NMR and ^{19}F NMR spectra of pure TFPPO and TFPPO with different perovskite precursor components. **b**, **c**, Pb 4*f* spectra (**b**) and Br 3*d* spectra (**c**) of control, TPPO-treated and TFPPO-treated RDPs. **d**, FTIR spectra of pure TPPO and TFPPO. **e**, FTIR spectra of control, TPPO-treated and TFPPO-treated RDPs.

Density functional theory simulations revealed that TFPPO formed hydrogen bonds with the ammonium tails of PEA in RDPs, increasing the binding energy by 0.65 eV (Extended Data Fig. 4).

Encouraged by the promising optical properties of these RDPs, next we sought to translate them into high-performance LEDs. We used a device configuration consisting of indium tin oxide (ITO, as the anode, about 32 nm)/poly(3,4-ethylenedioxythiophene)polystyrene sulfonate doped with nafion perfluorinated ionomer (PEDOT:PSS:PFI, as the hole-transport layer, about 210 nm)/RDPs (the active layer, about 60 nm)/tris[2,4,6-trimethyl-3-(pyridin-3-yl)phenyl]borane (3TPYMB, as the electron-transport layer, about 40 nm)/lithium fluoride (LiF, as the electron-injection layer, about 1 nm)/aluminium (Al, as cathode, about 150 nm) (Fig. 4a). The thickness of each functional layer was measured using transmission electron microscopy (TEM). We added poly(methylmethacrylate) (0.2 mg ml^{-1}) into the antisolvent to further improve the PLQY and film morphology of RDPs (Extended Data Fig. 3), which was enabled by the interaction between its carbonyl (C=O) groups and perovskite precursors during film deposition.

Control, TPPO-treated and TFPPO-treated RDP-based LEDs showed bright green emission with similar current–voltage characteristics, and TFPPO treatment enabled enhanced luminance (Fig. 4b, Extended Data Fig. 6a–c). Control and TPPO-treated RDP-based LEDs showed EQEs of 10.7% and 17.6%, respectively, while TFPPO-treated RDP-based LEDs achieved a high EQE of 25.6% (Fig. 4c)—close to the theoretical outcoupling efficiency obtained from optical modelling (Methods, Extended Data Fig. 7). The maximum current efficiency is 88 cd A^{-1}. We attribute the improved device performance to the superior PLQY combined with enhanced carrier balance in TFPPO-treated RDPs—these show similar hole-transport behaviour, and higher electron conductivity compared with control and TPPO-treated RDPs (Fig. 4d).

We then measured the device operating stability of LEDs based on TFPPO-treated RDPs, applying a constant current density of 8 mA cm^{-2}, which provided an initial luminance (L_0) of 7,200 cd m^{-2}, and monitoring the evolution of luminance. The half-life (T_{50})—the time by when L_0 decreased to half (L_0/2)—was 115 min (Fig. 4e), tenfold longer than that of the best previous reports at comparable initial luminance (Extended Data Table 1)[1,4–6,26–29].

In summary, RDPs with monodispersed QWs were synthesized using a bifunctional molecular additive that controlled the diffusion of the organic cations during film deposition, and also functioned as a surface passivant. This allowed us to fabricate compact, smooth and uniform RDP thin films with narrowband emission and high PLQY. We achieved RDP-based LEDs with an EQE of 25.6% with an average of 22.1 ± 1.2% over 40 devices, and an operating half-life of 115 min at an initial luminance of 7,200 cd m^{-2}, an order of magnitude longer than that of the best-known perovskite LEDs with EQEs exceeding 20% (refs. [1,4–6,26–29]).

Online content

Any methods, additional references, Nature Research reporting summaries, source data, extended data, supplementary information, acknowledgements, peer review information; details of author contributions and competing interests; and statements of data and code availability are available at https://doi.org/10.1038/s41586-021-03997-z.

1. Kim, Y.-H. et al. Comprehensive defect suppression in perovskite nanocrystals for high-efficiency light-emitting diodes. *Nat. Photon.* **15**, 148–155 (2021).
2. Hong, K., Le, Q. V., Kim, S. Y. & Jang, H. W. Low-dimensional halide perovskites: review and issues. *J. Mater. Chem. C* **6**, 2189 (2018).
3. Gao, X. et al. Ruddlesden–Popper perovskites: synthesis and optical properties for optoelectronic applications. *Adv. Sci.* **6**, 1900941 (2019).
4. Jiang, Y. et al. Reducing the impact of Auger recombination in quasi-2D perovskite light-emitting diodes. *Nat. Commun.* **12**, 336 (2021).
5. Kong, L. et al. Smoothing the energy transfer pathway in quasi-2D perovskite films using methanesulfonate leads to highly efficient light-emitting devices. *Nat. Commun.* **12**, 1246 (2021).
6. Sun, C. et al. High-performance large-area quasi-2D perovskite light-emitting diodes. *Nat. Commun.* **12**, 2207 (2021)
7. Jena, A. K., Kulkarni, A. & Miyasaka, T. Halide perovskite photovoltaics: background, status, and future prospects. *Chem. Rev.* **119**, 3036 (2019).
8. Xing, G. et al. Low-temperature solution-processed wavelength-tunable perovskites for lasing. *Nat. Mater.* **13**, 476–480 (2014).
9. Dou, L. et al. Solution-processed hybrid perovskite photodetectors with high detectivity. *Nat. Commun.* **5**, 5404 (2014).
10. Quan, L. N., Arquer, F. P. G., Sabatini, R. P. & Sargent, E. H. Perovskites for light emission. *Adv. Mater.* **30**, 1801996 (2018).
11. Shen, H. et al. Visible quantum dot light-emitting diodes with simultaneous high brightness and efficiency. *Nat. Photon.* **13**, 192–197 (2019).
12. Won, Y.-H. et al. Highly efficient and stable InP/ZnSe/ZnS quantum dot light-emitting diodes. *Nature* **575**, 634–638 (2019).
13. Ly, K. T. et al. Near-infrared organic light-emitting diodes with very high external quantum efficiency and radiance. *Nat. Photon.* **11**, 63–68 (2017).
14. Wu, T.-L. et al. Diboron compound-based organic light-emitting diodes with high efficiency and reduced efficiency roll-off. *Nat. Photon.* **12**, 235–240 (2018).
15. Cho, H. et al. Overcoming the electroluminescence efficiency limitations of perovskite light-emitting diodes. *Science* **350**, 1222 (2015).
16. Richter, J. M. et al. Enhancing photoluminescence yields in lead halide perovskites by photon recycling and light out-coupling. *Nat. Commun.* **7**, 13941 (2016).
17. Xing, G. et al. Transcending the slow bimolecular recombination in lead-halide perovskites for electroluminescence. *Nat. Commun.* **8**, 14558 (2017).
18. Miyata, A. et al. Direct measurement of the exciton binding energy and effective masses for charge carriers in organic-inorganic tri-halide perovskites. *Nat. Phys.* **11**, 582–587 (2015).
19. Quintero-Bermudez, R. et al. Compositional and orientational control in metal halide perovskites of reduced dimensionality. *Nat. Mater.* **17**, 900–907 (2018).
20. Ma, D. et al. Chloride insertion-immobilization enables bright, narrowband, and stable blue-emitting perovskite diodes. *J. Am. Chem. Soc.* **142**, 5126 (2020).
21. deQuilettes, D. W. et al. Photoluminescence lifetimes exceeding 8 μs and quantum yields exceeding 30% in hybrid perovskite thin films by ligand passivation. *ACS Energy Lett.* **1**, 438 (2016).
22. Braly, I. L. et al. Hybrid perovskite films approaching the radiative limit with over 90% photoluminescence quantum efficiency. *Nat. Photon.* **12**, 355–361 (2018).

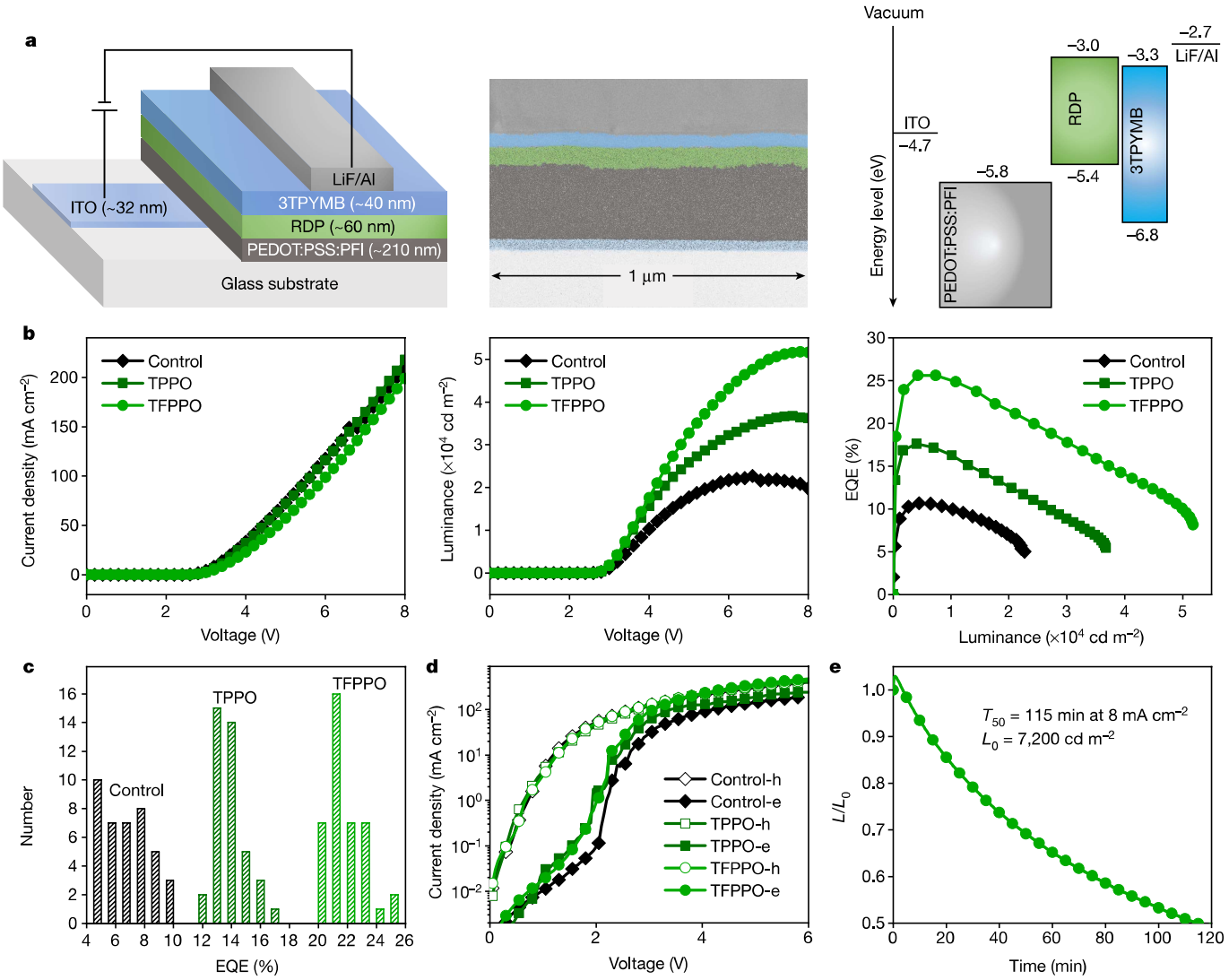

Fig. 4 | LED performance. a, Device structure (left), cross-sectional TEM image (middle) and energy band diagram (right). The energy levels of the RDPs were calculated from optical data and ultraviolet photoelectron spectroscopy (Extended Data Fig. 5). **b**, Current density versus voltage (left), luminance versus voltage (middle) and EQE versus luminance (right) curves. **c**, EQE histogram of 40 devices based on control, TPPO-treated and TFPPO-treated RDPs. **d**, Current density versus voltage curves of hole-only (h) and electron-only (e) devices based on control, TPPO-treated and TFPPO-treated RDPs. **e**, Operating stability of LEDs based on TFPPO-treated RDPs.

23. Lin-Vien, D., Colthup, N. B., Fateley, W. G. & Grasselli, J. G. in *The Handbook of Infrared and Raman Characteristic Frequencies of Organic Molecules* Ch. 16 (Academic Press, 1991).
24. Lin-Vien, D., Colthup, N. B., Fateley, W. G. & Grasselli, J. G. in *The Handbook of Infrared and Raman Characteristic Frequencies of Organic Molecules* Ch. 6 (Academic Press, 1991).
25. Lin-Vien, D., Colthup, N. B., Fateley, W. G. & Grasselli, J. G. in *The Handbook of Infrared and Raman Characteristic Frequencies of Organic Molecules* Ch. 3 (Academic Press, 1991).
26. Wang, H. et al. A multi-functional molecular modifier enabling efficient large-area perovskite light-emitting diodes. *Joule* **4**, 1977 (2020).
27. Dong, Y., et al. Bipolar-shell resurfacing for blue LEDs based on strongly confined perovskite quantum dots. *Nat. Nanotechnol.* **15**, 668–674 (2020).
28. Lin, K. et al. Perovskite light-emitting diodes with external quantum efficiency exceeding 20 per cent. *Nature* **562**, 245–248 (2018).
29. Shen, Y. et al. High-efficiency perovskite light-emitting diodes with synergetic outcoupling enhancement. *Adv. Mater.* **31**, 1901517 (2019).

Methods

Materials

Methylammonium bromide (MABr) and phenylethylammonium bromide (PEABr) were purchased from Dyesol. Cesium bromide (CsBr, 99.999%) was purchased from Alfa Aesar. Anhydrous dimethyl sulfoxide (DMSO), anhydrous chloroform, lead bromide ($PbBr_2$, >98%), triphenylphosphine oxide (TPPO, 98%), triphenylphosphine (TPP, >95%), tris(4-fluorophenyl)phosphine (TFPP), nafion perfluorinated resin solution (tetrafluoroethylene-perfluoro-3, 6-dioxa-4-methyl-7-octenesulfonic acid copolymer, 5 wt% in a mixture of lower aliphatic alcohols and water, containing 45% water) and lithium fluoride (LiF, >99.99%) were purchased from Sigma-Aldrich. Tris[2,4,6-trimethyl-3-(pyridin-3-yl)phenyl]borane (3TPYMB, >99%, sublimed) was purchased from Xi'an Polymer Light Technology. Poly(3,4-ethylenedioxythiophene)polystyrene sulfonate (PEDOT:PSS, Clevios PVP AI 4083) was purchased from Heraeus. All chemicals were used directly as received.

Synthesis and NMR characterization of TFPPO

TFPPO was synthesized through oxidization of TFPP. TFPP (2.0022 g, 6.33 mmol) was dissolved in 10 ml chloroform and reacted with an aqueous solution of H_2O_2 (30%, 10 ml) under stirring at room temperature overnight. The resulting mixture was extracted by chloroform and dried at 70 °C overnight to produce a white powder (0.9426 g, 2.84 mmol). Yield: 45%. ^{1}H NMR (499.87 MHz, DMSO-d_6) δ = 7.68 ppm (dtd, J = 11.5 Hz, 5.7 Hz, 2.1 Hz, 6H), 7.41 ppm (ddt, J = 8.9 Hz, 6.6 Hz, 2.1 Hz, 6H); ^{19}F NMR (470.30 MHz, DMSO-d_6) δ = −107.1 ppm; ^{31}P NMR (202.35 MHz, DMSO-d_6) δ = 23.69 ppm.

NMR measurements

One-dimensional ^{1}H NMR (^{1}H; 499.87 MHz), ^{19}F NMR (^{19}F; 470.30 MHz) and ^{31}P NMR (^{31}P; 202.35 MHz) spectra were acquired at 25 °C using a 500-MHz Agilent DD2 spectrometer equipped with a 5-mm ^{1}H–^{19}F{X} OneNMR probe. The spectra were acquired using the standard phosphorus pulse sequence as supplied by the Varian/Agilent acquisition software. The spectra were acquired with 32 scans, with a relaxation delay of 5 s, a receiver gain of 40 dB, an acquisition time of 20 s and a sweep width of 2,022, and the free induction decay was collected with 80,906 points.

RDP preparation

The perovskite precursor solution was prepared by dissolving $PbBr_2$ (0.6 mol l^{-1}), CsBr (0.32 mol l^{-1}), MABr (0.08 mol l^{-1}) and PEABr (0.4 mol l^{-1}) in anhydrous DMSO under continuous stirring overnight in a nitrogen-filled glovebox at room temperature. The resulting clear and colourless solution was diluted with 20 vol% DMSO, filtered and dripped onto the substrates, pre-spun at 1,000 r.p.m. for 10 s, then spin-cast at 5,000 r.p.m. for 60 s. Control, TPPO-treated and TFPPO-treated RDPs were prepared by dripping 0.5 ml antisolvent (pure chloroform, and chloroform with the addition of 10 mg ml^{-1} TPPO or TFPPO) after 20 s during the second step. Finally, the thin films were annealed on a hot plate at 90 °C for 5 min to remove the residual solvents.

GIWAXS measurements

GIWAXS images were collected at beamline 7.3.3 of the Advanced Light Source at Lawrence Berkeley National Laboratory. Two-dimensional scattering was collected at 0.1° and 0.5° incidence with 10-keV X-rays and recorded on a Pilatus 2M camera (172-μm pixel size, 1,475 × 1,679 pixels). Data processing was performed using Nika and GIXSGUI software packages[30,31].

TA measurements

A regeneratively amplified Yb:KGW laser (PHAROS, Light Conversion) was used to generate femtosecond laser pulses at a wavelength of 1,030 nm as the fundamental beam with a repetition rate of 5 kHz. The fundamental beam was passed through a beam splitter, where the majority of the beam was used to pump an optical parametric amplifier (ORPHEUS, Light Conversion) to serve as a narrowband pump (pulse duration of about 200 fs, full-width at half-maximum of about 10 nm). The remaining part of the beam was focused into a translating sapphire crystal to generate a white light probe ranging between 400 nm and 800 nm. The pump and probe pulses were directed into a commercial TA spectrometer (Helios, Ultrafast). The probe pulse was sent to a retroreflector mounted on a delay stage where multiple reflections off the retroreflector allowed for a delay relative to the pump pulse of up to 8 ns. TA measurements were obtained with pump powers at 70 μW, and a spot size of 0.3 μm^2 (assuming a Gaussian beam profile).

PL characterization

A Horiba Fluorolog system was used for PL characterization. Steady-state PL was measured with a monochromatized xenon lamp as the excitation source. A time-correlated single-photon counting detector and a pulsed laser diode (wavelength λ = 374 nm) were used to acquire transient PL. An instrument response function of Δt = 0.13 ns provided a limit to the overall time resolution. Time-resolved PL decay curves were recorded by measuring individual transient PL traces at increasing emission wavelengths. Ultraviolet–visible absorption, excitation power-dependent PLQY and photostability were measured in a nitrogen-filled glovebox, using the QE Pro65 spectrometer (Ocean Optics) and a laser diode (λ = 365 nm) as the excitation light source system, and the system was calibrated with the aid of a standard halogen lamp (HL-3-INT-CAL, Ocean Optics).

XRD measurements

XRD measurements were conducted using a Rigaku MiniFlex 600 diffractometer (Bragg-Brentano geometry) equipped with a NaI scintillation counter detector and a monochromatized Cu Kα radiation source (λ = 1.5406 Å) operating at a voltage of 40 kV and a current of 15 mA.

SEM measurements

We prepared RDP thin films on ITO-coated glass substrates in a nitrogen-filled glovebox, put them into a sealable sample tray, and transferred it to the field emission scanning electron microscope (FESEM, JSM-7610F) to characterize the surface morphology. The measurements were operated at a voltage of 2 kV.

AFM measurements

AFM measurements were performed using an Asylum Research Cypher AFM operated in a.c. mode in air conditions. Images were collected using ASYELEC-02 silicon probes with titanium-iridium coatings from Asylum Research. The probes had a typical spring constant of 42 N m^{-1}.

XPS measurements

We prepared RDP thin films on ITO-coated glass substrates in a nitrogen-filled glovebox. Thermo Scientific K-Alpha+ XPS system was used for XPS analysis of Pb 4*f* and Br 3*d* chemical states. The excitation source was Al Kα (1,486.6 eV).

FTIR measurements

FTIR measurements were performed using the Thermo Scientific Nicolet iS50 ATR-FTIR. The samples were fabricated on glass substrates and placed on top of the attenuated total reflectance crystal. The spectra were obtained using 16 scans with a resolution of 4 cm^{-1}, and the collection wavenumber range was between 400 cm^{-1} and 4,000 cm^{-1}.

Density functional theory calculations

Density functional theory calculations were performed using the Vienna Ab initio Simulation Package (VASP)[32] using an energy cut-off of 520 eV for the planewave basis set, the Perdew–Burke–Ernzerhof[33]

exchange-correlation functional and projector-augmented-wave Perdew–Burke–Ernzerhof pseudopotentials[34,35]. Layered RDPs with $n = 5$ were modelled using MA as a cation both inside and on the surface. The slabs of layered perovskites are separated by 20 Å of vacuum in the x direction and are periodic in the y direction and z direction with only the Γ k-point being used for simulations. All geometries were relaxed until forces on atoms converged to below 1 meV Å^{-1}, including cell-size degrees of freedom. Binding energies were then calculated as a difference between $E_{\text{slab+molecule}}$, E_{slab} and $E_{\text{molecule in gas phase}}$.

TEM measurements

We prepared the device cross-sectional samples using a focused-ion-beam system (FIB, FEI Scios 2 Hivac). The protective layers of gold and platinum were deposited before ion-beam cutting and etching. The voltage used in the ion-beam etching process was 30 kV (0.1 nA), and the purge was 5 kV (0.1 nA). We characterized bright-field and element-mapping images using FEI Talos F200X G2 TEM.

Ultraviolet photoelectron spectroscopy measurements

We prepared RDP thin films on ITO-coated glass substrates in a nitrogen-filled glovebox. Photoelectron spectroscopy was performed in a PHI5500 Multi-Technique system using non-monochromatized He Iα radiation ($h\upsilon$ = 21.22 eV). All work function and valence band measurements were performed at a take-off angle of 88°, with a base chamber pressure of 10^{-7} Pa. A bias of −15 V was applied to measure the work function.

LED fabrication

LEDs were fabricated on patterned ITO-coated glass substrates (Thin Film Devices). The thickness of the glass substrate is 0.70 mm. The thickness of the ITO layer is 320 ± 25 Å and the resistivity is 100 ± 25 Ω sq^{-1}. We cleaned the substrates using detergent, deionized water, acetone and isopropanol in an ultrasonic washer, then treated them with oxygen plasma for 5 min. Then a mixed solution of PEDOT:PSS and PFI (at a mass ratio of 1:1) was spin-cast at 500 r.p.m. for 10 s, then 4,500 r.p.m. for 90 s, followed by annealing on a hot plate at 150 °C for 20 min in air conditions. The substrates were cooled and transferred into a nitrogen-filled glovebox, then the RDP thin films were fabricated thereon as described above, except that 0.2 mg ml^{-1} poly(methylmethacrylate) (PMMA) was added into the antisolvent. Finally, the substrates were transferred into a high-vacuum thermal evaporator, where 3TPYMB (approximately 40 nm), LiF (approximately 1 nm) and Al (approximately 150 nm) were deposited layer by layer through a shadow mask at a pressure below 10^{-4} Pa.

LED evaluation

The device active area was 5.25 mm^2 as defined by the overlapping area of the ITO and aluminium electrodes. We used the LED measurement method of Forrest et al.[36], at room temperature in a nitrogen-filled glovebox. We first measured the angular dependence of the electroluminescence (EL) intensity and spectra, and found that the light distribution was consistent with a Lambertian circle and that the EL spectra are independent of the angle (Extended Data Fig. 6d, e). The light distribution was measured by using a Hamamatsu PMA-12 detector, coordinating with a stepping motor controller (Hamamatsu DS-102) to automatically change the angle from 0° to 90°. The device was operated under a fixed bias of 4 V. The current–voltage characteristics were measured using a Keithley 2400 source meter. The absolute radiation flux for calculating the EQE, power efficiency and luminance was collected using an integrating sphere and a QE Pro65 spectrometer (Ocean Optics). We used commercial organic light-emitting diodes (OLEDs, Visionox Technology) as calibration sources to cross-check the LED measurements. We carried out the analysis in our lab, and secured an independent analysis at the National Institute of Metrology of China, from which we now show the results that accord with one another to within 5% relative (Extended Data Fig. 6f).

LED stability measurements

The device operating stability was measured at room temperature in a nitrogen-filled glovebox. LEDs were driven using a Keithley 2400 source meter at a constant current, and the EL intensity was measured with a commercial photodiode (Vishay Semiconductors BPW34). We measured the operating stability of LEDs based on TFPPO-treated RDPs, applying a constant current density of 8 mA cm^{-2} and monitoring the evolution of luminance.

Hole-only and electron-only device fabrication

The hole-only devices were fabricated with the structure ITO/PEDOT:PSS:PFI (approximately 210 nm)/RDP (approximately 60 nm)/MoO_x (approximately 30 nm)/Al (approximately 150 nm). The electron-only devices were fabricated with the structure ITO/3TPYMB (approximately 150 nm)/RDP (approximately 60 nm)/3TPYMB (approximately 40 nm)/LiF (approximately 1 nm)/Al (approximately 150 nm). PEDOT:PSS:PFI, RDP, 3TPYMB, LiF and Al were prepared as described above, and MoO_x was deposited at a pressure below 10^{-4} Pa in a high-vacuum thermal evaporator.

Spectroscopic ellipsometry analysis

TFPPO-treated RDPs were prepared on sapphire substrates to measure ellipsometric parameters, amplitude ratio Ψ and phase difference Δ, which were collected at incident angles of 60°, 65° and 70° using an ellipsometer (Wuhan Eoptics Technology). To achieve the extinction coefficient and refractive index, experimental Ψ and Δ spectra were fitted with an optical model by varying free parameters (dispersion model parameters and layer thickness). The Cauchy dispersion function was utilized to describe the optical property of the sapphire substrate. TFPPO-treated RDPs were described using the Tauc–Lorentz model[37]. The dielectric function of the PEDOT:PSS:PFI layer was described using several Gaussian oscillators. Optical constants, extinction coefficient, and real and imaginary reflective indices were relative to the dielectric function. The goodness of fit of the optical model was defined using the lowest mean-squared error[38].

Device optical modelling

To evaluate the theoretical outcoupling efficiency, we built models to study the influence of nanostructure at the interface of POEDT:PSS:PFI and the RDP-based active layer in LEDs. This model considered the output light-wave power excited by a uniform plane of dipole sources located within the active layer, which was sandwiched among a stack of functional layers of varying complex refractive indices. The photons were modelled as though they were generated by spontaneous emission within the active layer with random direction and polarization. To calculate the average generated electromagnetic field intensity and the power dissipation channels of the dipole sources, we averaged over the dipole orientation and polarizations. Similar assumptions have been made in other studies[39,40]. The morphology of the PEDOT:PSS:PFI layer was characterized using SEM and AFM, the thickness of each layer was determined using TEM, and the corresponding refractive indices were measured using ellipsometry (Extended Data Fig. 7a, b). The optical simulations were performed using the Chance–Prock–Silbey model by the integrated commercial software of Setfos (5.05 from Fluxim AG). After construction of the geometrical dimension of the LED, respective refractive indices and EL spectra were imported into the model. All layers except for the active layer were evaluated with complex refractive indices. The glass substrate was set to be incoherent due to its large thickness.

The power dissipation channels were examined using mode analysis that included the outcoupling mode (direct emission), substrate mode, guided mode, absorption loss and evanescent coupling. These channels are widely used for the description of the power dissipation, both qualitatively and quantitatively in perovskite and quantum dot LEDs,

and were originally defined and classified in OLEDs by their in-plane wave vectors[41]. As the light emission from the aluminium cathode side was negligible, the outcoupling power mainly originated from the glass side of the device. Light energy loss due to the complex refractive indices of the layers was considered as intrinsic optical absorption. If the in-plane wavevector k_x of light was larger than the wavevector in free space k_{free} and smaller than the wavevector in the substrate $n_{glass}k_{free}$, this part of light energy was considered trapped in the substrate mode; if the light with k_x was larger than $n_{glass}k_{free}$ and smaller than the equivalent wavevector in the active and the transport layers $n_{effective}k_x$, this part of energy was considered as trapped in the guided mode; if the light with k_x was larger than $n_{effective}k_x$, and was emitted with an imaginary angle, it was classified as the evanescent coupling to represent evanescent wave propagating along the interfaces and/or plasmons in the metal layer.

The EQE is equal to the product of internal quantum efficiency (IQE) and light extraction efficiency (LEE) as EQE = IQE × LEE, where IQE is a product of internal radiative efficiency η_{rad} and the charge balance efficiency η_{inj} (ref. [42]). The LEE evaluates the portion of the escaped photons outside the LED to the total emitted photons generated in the active layer. The outcoupling efficiency in our model was defined as the number of outcoupling photons over the total generated photons in the active layer, and was calculated using Setfos. Therefore, the outcoupling efficiency can be considered equal to the LEE. Following the nomenclature of mode analysis in the above paragraph, we also used the outcoupling efficiency instead of LEE when analysing the power dissipation channel of the LEDs. Assuming near-unity η_{rad} and η_{inj}, EQE will become equal to LEE, and accordingly the value of outcoupling efficiency can be used to evaluate the EQE.

Extended Data Fig. 7c describes the power dissipation channels of planar LEDs as a function of the equivalent recombination centre location (ERCL), which was numerically evaluated by the ratio of the position of the plane of the dipole sources to the overall thickness of the active layer. The ERCL ranged from 0 to 1 corresponding to the top (close to hole-transport layer, HTL) and bottom (close to the electron-transport layer, ETL) of the active layer. A noticeable feature was the significant change of the evanescent coupling when the ERCL was at the top of the active layer, due to the strong excitation of the electromagnetic (evanescent and/or plasmonic) modes propagating along the interfaces of functional layers. As the thickness of each functional layer remained constant, the absorption loss and the total trapped light energy (energy trapped inside the active layer and the substrate) showed little variation as the ERCL approached the ETL. As the ERCL was shifted from 0 to 1, the outcoupling energy gradually increased to 20.3% (for an ERCL of 0.56) and then decreased to 18.4%. The outcoupling efficiency spectra were also evaluated as a function of the ERCL. We found that close to the HTL, the outcoupling efficiency was lower across the entire emission spectra. Conversely, the optimal recombination centre location led to the highest outcoupling efficiency in the emission spectra.

In addition to the influence of the ERCL, the outcoupling efficiency was influenced by the scattering interface as it could randomize the propagation angle of the photons and extract the photons from trapped modes. Therefore, a randomly nanostructured interface was added between the HTL and TFPPO-treated RDPs to simulate scattering. Compared with its planar counterpart, the light energy was no longer trapped in the guided mode. As the interface between the glass substrate and the air was still optically flat in the model as in the planar device, there was noticeable amount of energy trapped inside the substrate mode. The absorption loss was also decreased, as more light could escape outside the device by scattering without being trapped and absorbed by the transport layers with complex refractive indices. The effective scattering interface led to a clear improvement of the outcoupling efficiency compared with the planar device. For lower ERCLs, the plane of the dipole sources was closer to the HTL, resulting in stronger scattering influence and a higher outcoupling efficiency over 30%.

Data availability

The data that support the findings of this study are available from the corresponding authors.

30. Ilavsky, J. Nika: software for two-dimensional data reduction. *J. Appl. Cryst.* **45**, 324 (2012).
31. Jiang, Z. GIXSGUI: a MATLAB toolbox for grazing-incidence X-ray scattering data visualization and reduction, and indexing of buried three-dimensional periodic nanostructured films. *J. Appl. Cryst.* **48**, 917 (2015).
32. Kresse, G. & Furthmüller, J. Vienna Ab-Initio Simulation Package (VASP) (Vienna Univ., 2001).
33. Perdew, J. P.; Burke, K., Ernzerhof, M. Perdew, Burke, and Ernzerhof reply. *Phys. Rev. Lett.* **80**, 891 (1998).
34. Kresse, G. & Joubert, D. From ultrasoft pseudopotentials to the projector augmented-wave method. *Phys. Rev. B* **59**, 1758 (1999).
35. Blöchl, P. E. Projector augmented-wave method. *Phys. Rev. B* **50**, 17953 (1994).
36. Forrest, S. R., Bradley, D. D. C. & Thompson, M. E. Measuring the efficiency of organic light-emitting devices. *Adv. Mater.* **15**, 1043 (2003).
37. Li, H. et al. A review of characterization of perovskite film in solar cells by spectroscopic ellipsometry. *Sol. Energy* **212**, 48 (2020).
38. Jellison, G. E. Jr Data analysis for spectroscopic ellipsometry. *Thin Solid Films* **234**, 416 (1993).
39. Zhao, B. et al. High-efficiency perovskite-polymer bulk heterostructure light-emitting diodes. *Nat. Photon.* **12**, 783–789 (2018).
40. Meng, S.-S., Li, Y.-Q. & Tang, J.-X. Theoretical perspective to light outcoupling and management in perovskite light-emitting diodes. *Org. Electron.* **61**, 351 (2018).
41. Zhu, R., Luo, Z. & Wu, S.-T. Light extraction analysis and enhancement in a quantum dot light emitting diode. *Opt. Express* **22**, A1783 (2014).
42. Cho, C. et al. The role of photon recycling in perovskite light-emitting diodes. *Nat. Commun.* **11**, 611 (2020).

Acknowledgements This publication is based in part on work supported by the Natural Sciences and Engineering Research Council of Canada (NSERC, number 537463-18), the National Natural Science Foundation of China (numbers 51802102, 21805101, 51902110 and 61905107), the Natural Science Foundation of Fujian Province (numbers 2020J06021 and 2019J01057) and the National Key R&D Program of China (number 2019YFB1704600). We also acknowledge Huawei Canada for financial support and thank C. Zhu of the Advanced Light Source for assistance with GIWAXS measurements; G. Xing and J. Guo at University of Macau for LED light distribution measurements; C. Cui, S. Bian and J. Lu at Huaqiao University for optical constant measurements; and the National Institute of Metrology (NIM) of China for cross-checking LED measurements.

Author contributions E.H.S. and Z.W. supervised the project. D.M. and E.H.S. conceived the idea, designed the experiments and wrote the manuscript. D.M. and Y.K. synthesized and purified TFPPO. D.M. and K.L. prepared the RDP thin films, performed XPS and PL characterization, and fabricated LEDs. D.M., Y.D. and Y.L. performed TA measurements. H.C. performed DFT calculations. A.H.P. and A.J. performed GIWAXS measurements. D.W. performed optical modelling. Y.-K.W. performed XRD and AFM measurements. K.L. and B.C. performed SEM and TEM measurements. D.M., K.L., F.Y., Z.-H.L. and Z.W. performed LED measurements. P.L. performed ultraviolet photoelectron spectroscopy measurements. J.Z.F. performed FTIR measurements. Y.K. analysed the NMR data. All authors discussed the results and commented on the paper.

Competing interests The authors declare no competing interests.

Additional information

Correspondence and requests for materials should be addressed to Zhanhua Wei or Edward H. Sargent.

Peer review information *Nature* thanks Tae-Woo Lee, Henry Snaith and the other, anonymous, reviewer(s) for their contribution to the peer review of this work.

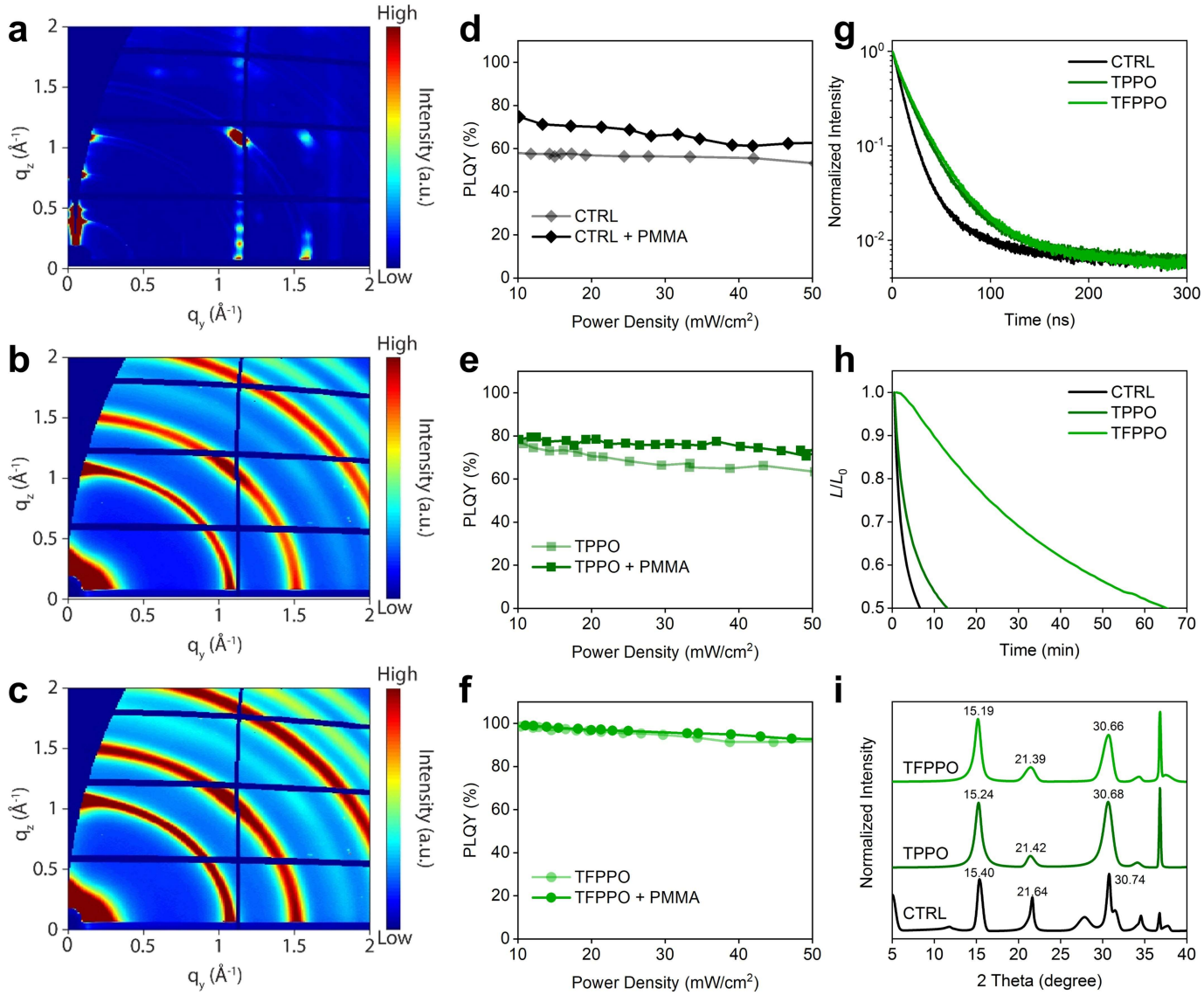

Extended Data Fig. 1 | Characteristics of control, TPPO-treated and TFPPO-treated RDPs. a–c, GIWAXS profiles. **d–f**, Excitation power-dependent PLQY of control, TPPO-treated and TFPPO-treated RDPs with and without PMMA additives. **g**, Time-resolved PL decay curves. **h**, Photostability under continuous excitation using a laser diode (365 nm, about 180 mW cm^{-2}) in a nitrogen-filled glovebox. The half-lives are 6 nm, 13 nm and 65 min, respectively. **i**, XRD profiles. The crystallite sizes calculated using the Scherrer equation are 11.4 nm, 7.5 nm and 6.5 nm, respectively.

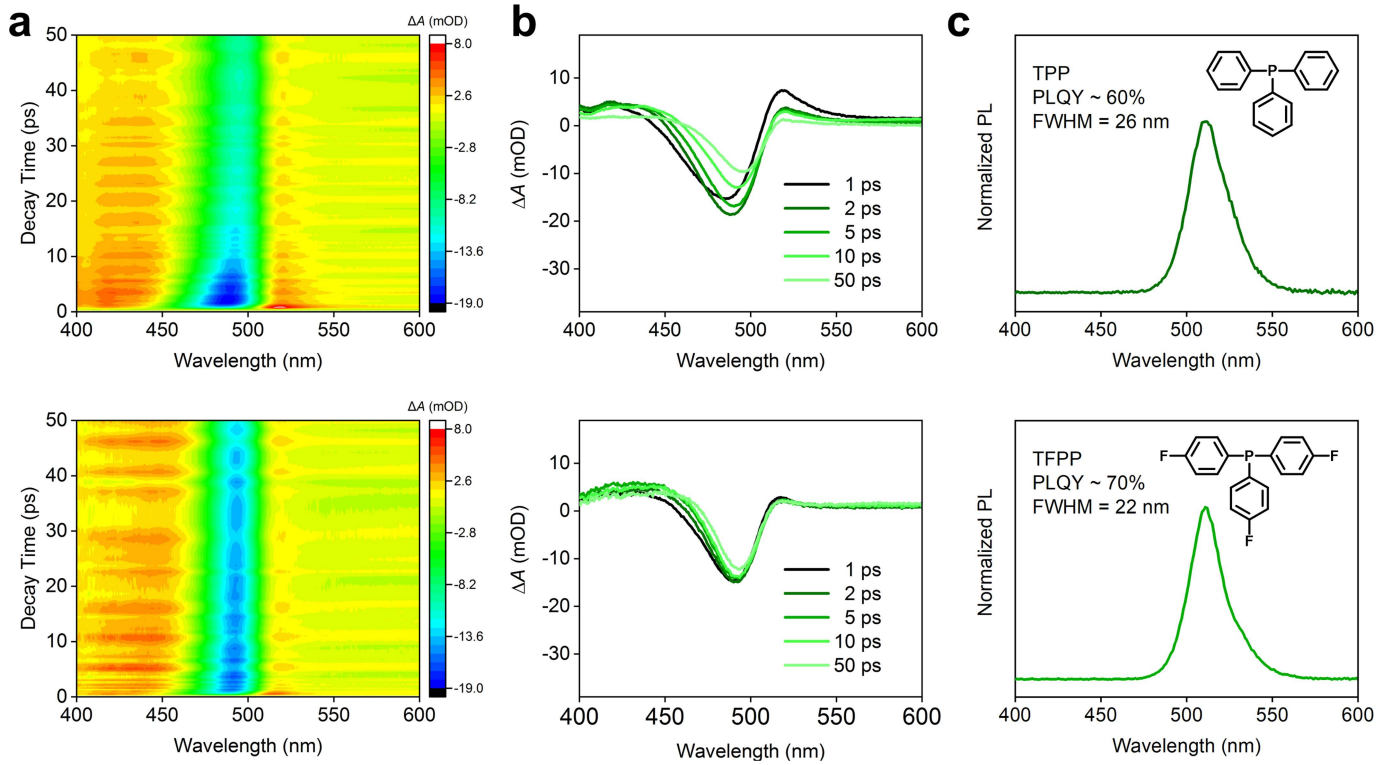

Extended Data Fig. 2 | Optical characteristics of TPP-treated and TFPP-treated RDPs. a, TA spectra at a delay time ranging from 0 ps to 50 ps. **b**, TA spectra at delay times of 1 ps, 2 ps, 5 ps, 10 ps and 50 ps. **c**, PL spectra. The inset shows the chemical structure of TPP and TFPP, respectively.

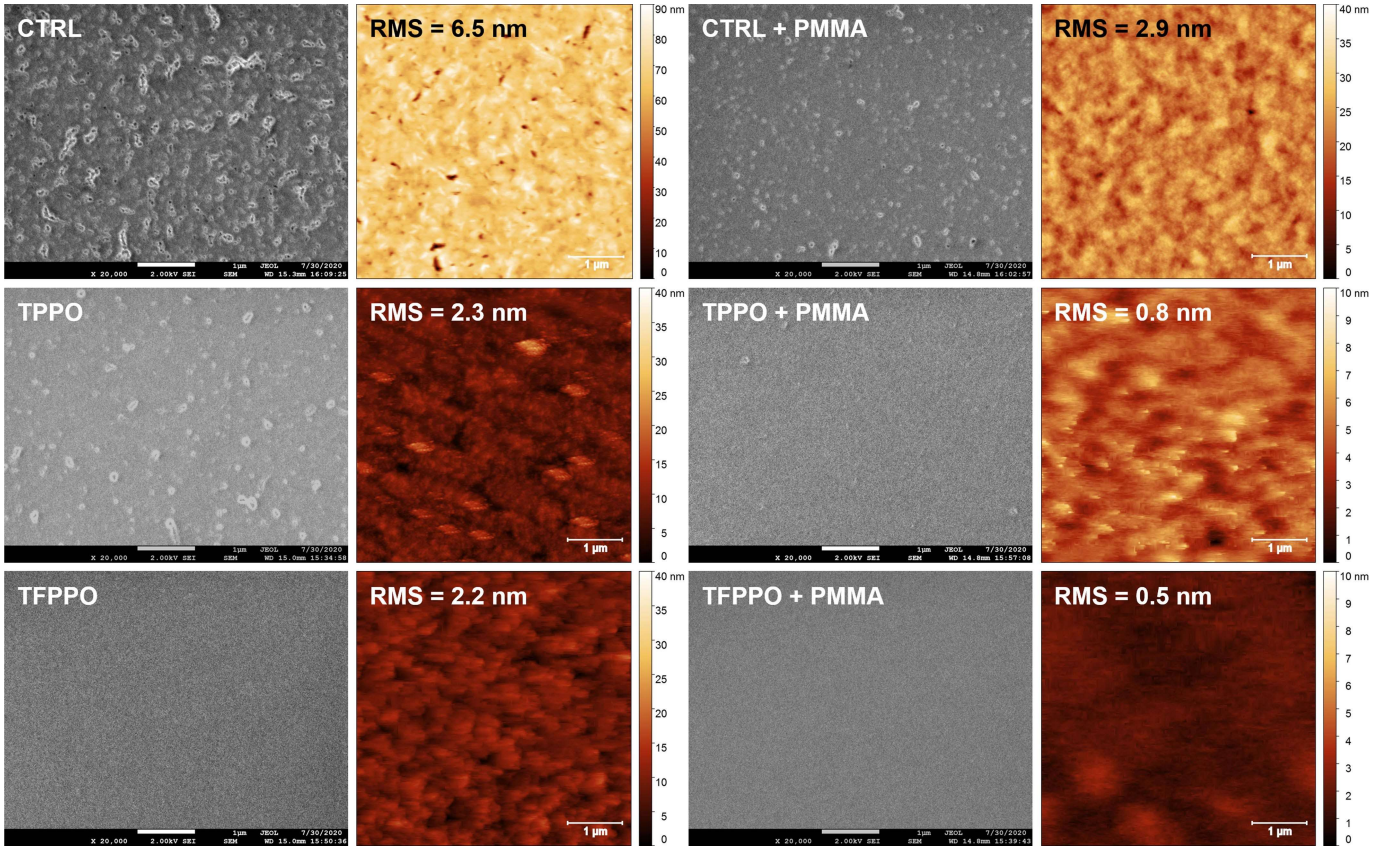

Extended Data Fig. 3 | Film morphology. Top-view SEM and AFM images of control, TPPO-treated and TFPPO-treated RDP thin films with and without PMMA additives.

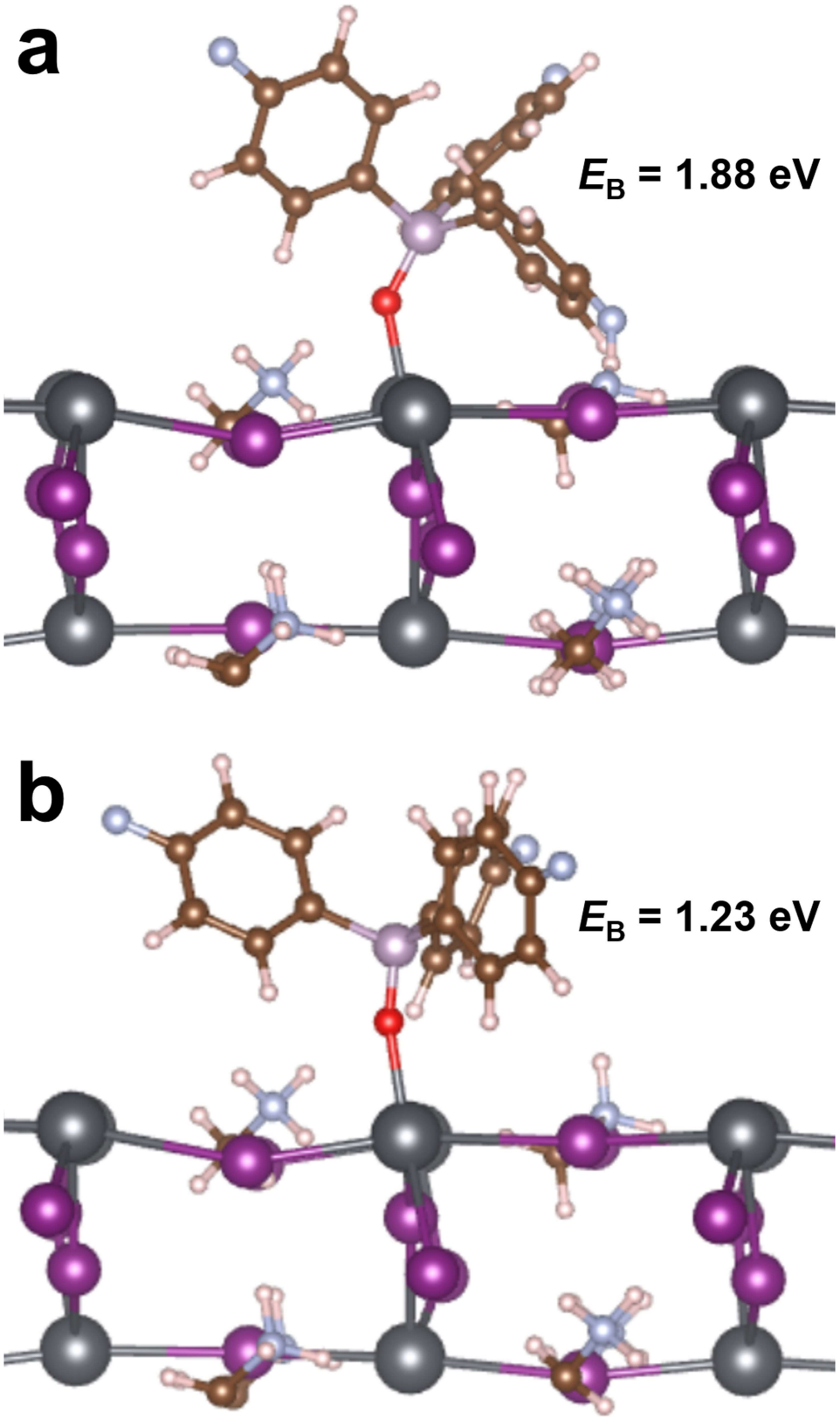

Extended Data Fig. 4 | Density functional theory simulations. a, TFPPO binding with the unsaturated lead dangling bonds at the perovskite edge through P=O:Pb and forming hydrogen bonds with the ammonium tails of the PEA organic cations (N-H···F) shows a binding energy of 1.88 eV. **b**, TFPPO with only P=O:Pb (no N-H···F) shows a binding energy of 1.23 eV.

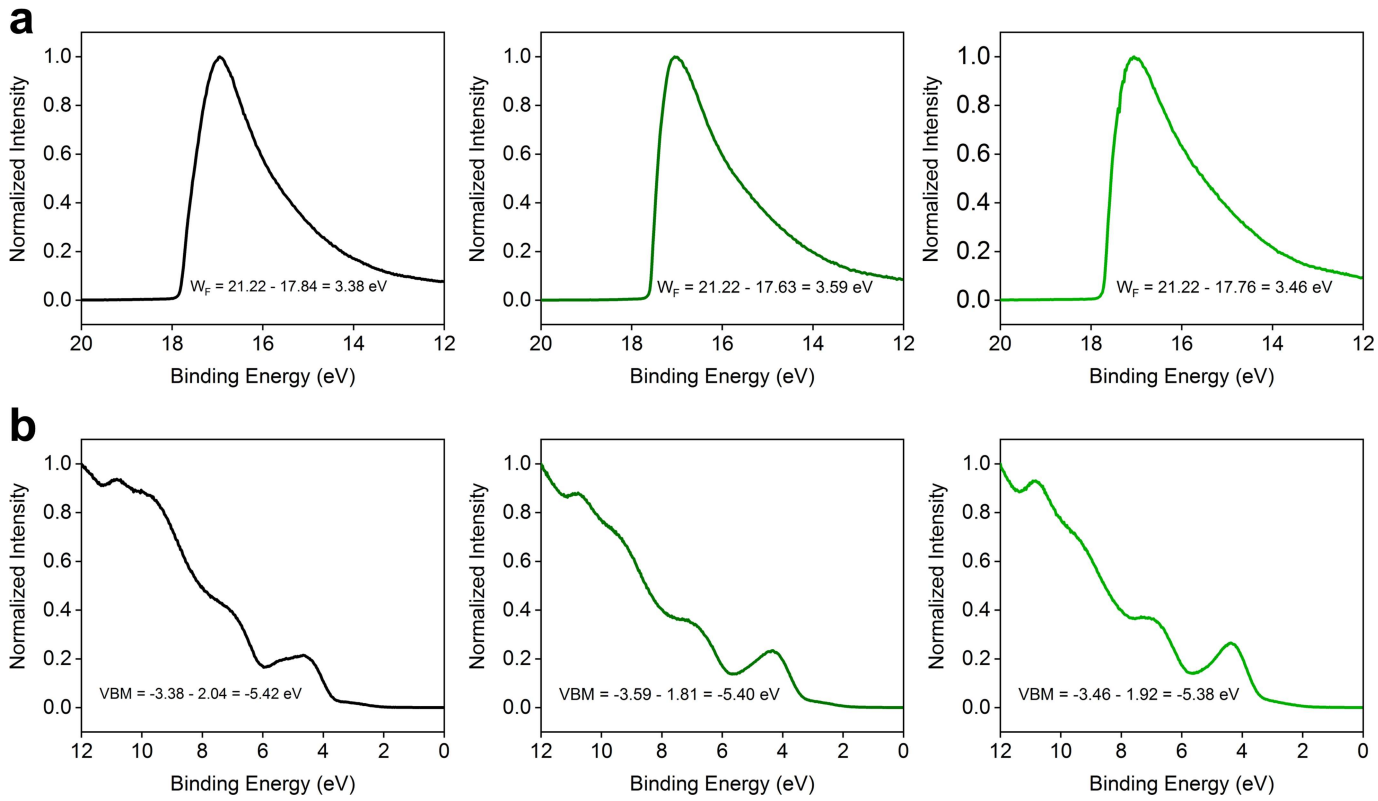

Extended Data Fig. 5 | Ultraviolet photoelectron spectroscopy characteristics. a, Second electron cut-off. **b**, Valence band spectra of control, TPPO-treated and TFPPO-treated RDPs (from left to right).

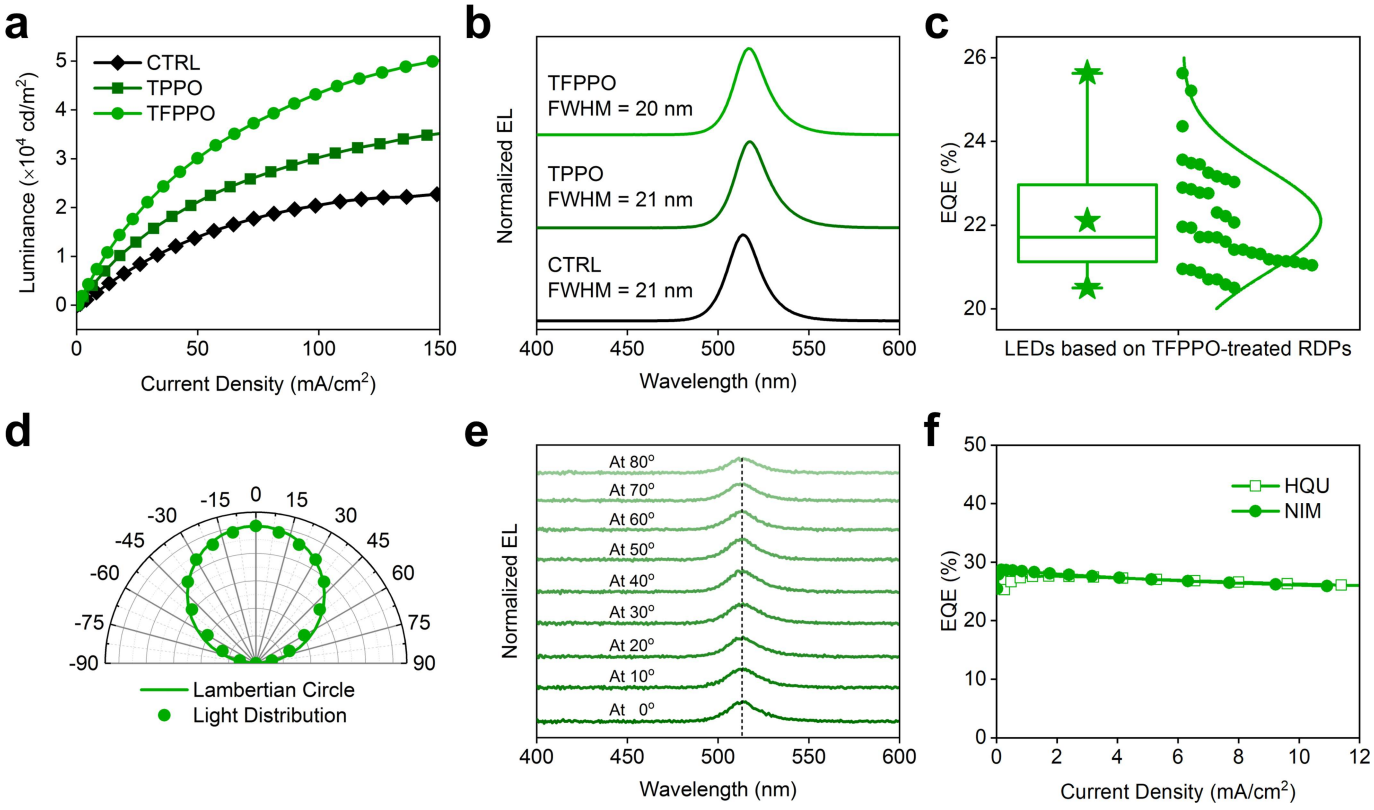

Extended Data Fig. 6 | Supplementary LED characteristics. a, Luminance versus current density curves; **b**, EL spectra of LEDs based on control, TPPO-treated and TFPPO-treated RDPs. **c**, Box plot of 40 devices based on TFPPO-treated RDPs (made across four batches). **d**, **e**, Angle-dependent EL intensity and spectra of LEDs based on TFPPO-treated RDPs. **f**, EQE versus current density curves of commercial OLEDs measured in our lab at Huaqiao University (HQU) and at the National Institute of Metrology (NIM) of China.

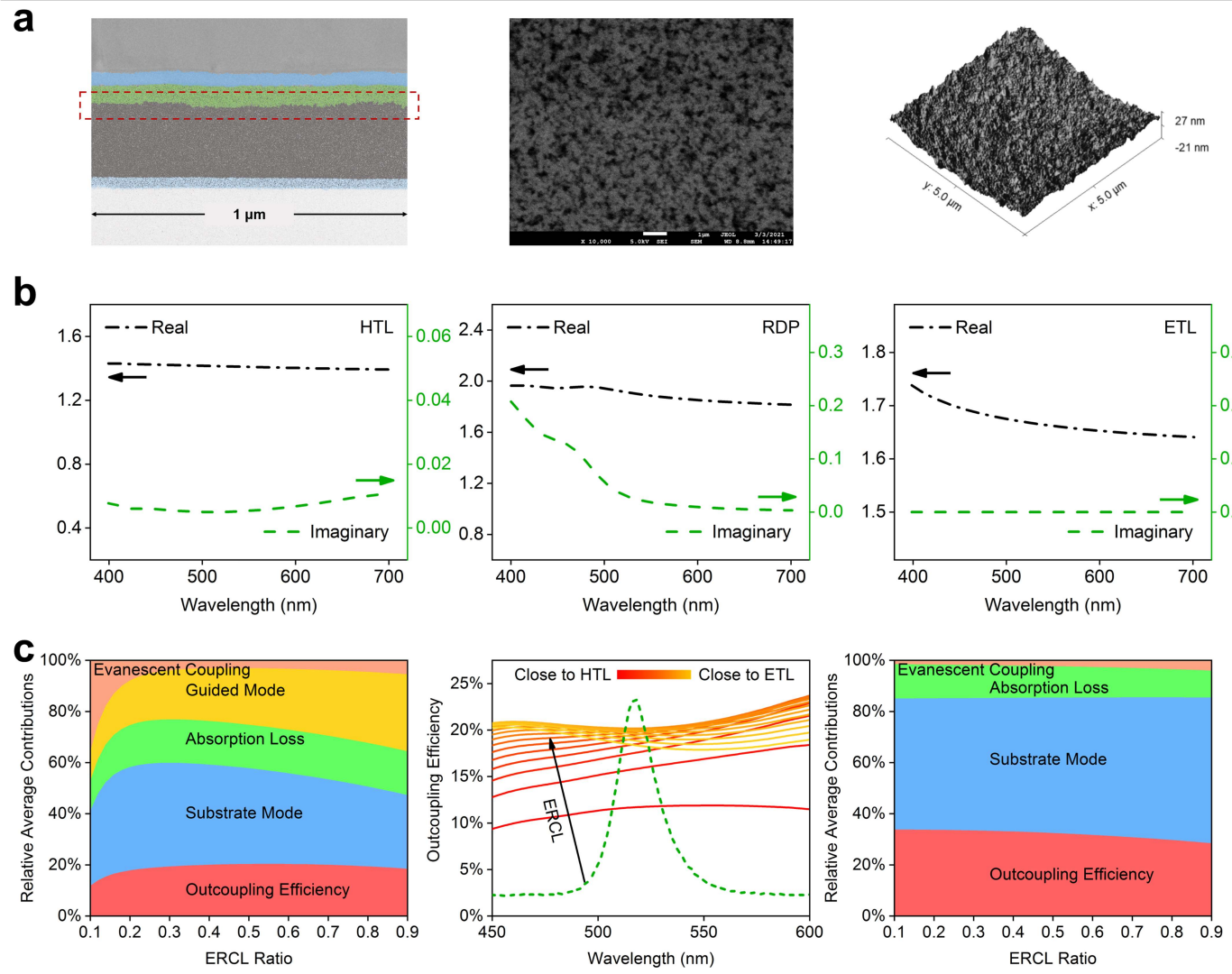

Extended Data Fig. 7 | Optical modelling. a, TEM image of LEDs based on TFPPO-treated RDPs, top-view SEM and AFM images of the PEDOT:PSS:PFI layer on ITO substrates. **b**, Refractive indices of the HTL, RDP and ETL layers for numerical simulations. **c**, Power dissipation channels for planar LEDs (left), outcoupling efficiency of planar LEDs as a functional of ERCL (middle) and power dissipation channels for LEDs with a randomly-nanostructured interface between HTL and RDPs (right).

Extended Data Table 1 | Performance of reported green perovskite LEDs having EQE exceeding 20%

Perovskites	EQE_{max} (%)	$EQE_{average}$ (%)	L_{max} (cd m^{-2})	λ_{EL} (nm)	FWHM (nm)	Operating stability	Reference
Perovskite Nanocrystals: $CsPbBr_3$	20.1	19.0	6.0×10^3	531	20	T_{50} = 174 min (L_0 = 100 cd m^{-2})	*Joule* **2020**, *4*, 1977
Perovskite Nanocrystals: $CsPbBr_3$ with bipolar shell	22.0	17.0	$\sim10^3$	505	18	T_{50} = 60 min (L_0 = 1,200 cd m^{-2})	*Nat. Nanotechnol.* **2020**, *15*, 668
Perovskite Nanocrystals: $FA_{0.9}GA_{0.1}PbBr_3$	23.4	Not Mentioned	2.4×10^4	530	20	T_{50} = 7 min (L_0 = 1,000 cd m^{-2})	*Nat. Photon.* **2021**, *15*, 148
3D Perovskites: $CsPbBr_3$ + MABr	20.3	Not Mentioned	1.4×10^4	525	20	T_{50} = 10 min (L_0 = 3,800 cd m^{-2})	*Nature* **2018**, *562*, 245
3D Perovskites: $CsPbBr_3$	20.3	Not Mentioned	2.5×10^4	514	18	Not Mentioned	*Adv. Mater.* **2019**, 1901517
RDP: *p*-$FPEA_2MA_2Pb_3Br_{10}$ + CF_3KO_3S	20.4	Not Mentioned	8.2×10^4	526	21	T_{50} = 6.5 min (L_0 = 10,000 cd m^{-2})	*Nat. Commun.* **2021**, *12*, 336
RDP: $BTA_{0.4}Cs_{1.2}PbBr_{3.6}$ + CsMeS	20.5	17.1±1.7	1.3×10^4	512	22	T_{50} = 25 min (L_0 = 1,000 cd m^{-2})	*Nat. Commun.* **2021**, *12*, 1246
RDP: $PEA_2(FA_{0.7}Cs_{0.3})_2Pb_3Br_{10}$	21.3	19.3	1.7×10^4	520	21	T_{50} = 120 min (L_0 = 100 cd m^{-2})	*Nat. Commun.* **2021**, *12*, 2207
RDPs: $PEA_2Cs_{1.6}MA_{0.4}Pb_3Br_{10}$	**25.6**	**22.1±1.2**	**5.2×10^4**	**517**	**20**	**T_{50} = 115 min (L_0 = 7,200 cd m^{-2})**	**This work**

EQE_{max}, maximum external quantum efficiency; $EQE_{average}$, average external quantum efficiency; L_{max}, maximum luminance; λ_{EL}, EL wavelength; FWHM, full-width at half maximum; T_{50}, device operating half-life; L_0, initial luminance.